Improving Reliability of Heat Transfer and Materials Flow Calculations during Friction Stir Welding of Dissimilar Aluminum Alloys

Friction, slip between the tool and the workpiece, heat transfer at the bottom surface, and internal heat generation were studied for their effects on model reliability

BY R. NANDAN, B. PRABU, A. DE, AND T. DEBROY

ABSTRACT. The temperature fields, cooling rates, torque on the tool, stir zone geometry, and the magnesium concentration profiles were examined experimentally and theoretically for the friction stir welding (FSW) of AA 1200 and AA 6061 dissimilar aluminum alloys. The thermal cycles, torque on the tool, and the magnesium concentration profiles were experimentally determined for various welding conditions. A heat, momentum, and solute transport model based on a rectangular fixed grid finite difference method was developed. Four important parameters, friction coefficient, the extent of sticking, heat transfer coefficient at the bottom surface, and the extent of viscous dissipation converted to heat significantly affected both the temperature fields and the torque on the tool. The reliability of the model predictions was improved by optimizing these four parameters that cannot be prescribed either from the welding conditions or from fundamental principles, using a genetic algorithm and measured thermal cycles and torques for different welding conditions. The magnesium concentration profiles showed that the plasticized materials moved in layers without significant diffusive interlayer mixing. The computed results showed that the extent of viscous dissipation converted to heat was fairly low consistent with limited atomic mixing. The optimized values of the extent of slip between the tool and the workpiece indicated extensive sticking for various welding conditions. The approach to determine values of uncertain

parameters led to reliable model predictions as evidenced by good agreement between both the experimentally measured and computed torque values and thermal cycles.

Introduction

In recent years, numerical models have provided significant quantitative understanding of the welding processes and welded materials that could not have been possible otherwise. Apart from the calculation of temperature and velocity fields, these models have been used to calculate various important features of welding. These include the weld pool shape and size (Refs. 1, 2), solidified surface profiles (Ref. 1), cooling rates (Ref. 1), solidification characteristics (Ref. 2), grain structure (Refs. 3–5) and topology (Ref. 6), phase transformation kinetics (Refs. 7–9), inclusion structure (Ref. 10), weld metal composition change owing to both the evaporation of alloying elements (Refs. 11–15) and the dissolution of gases (Refs. 16, 17), and for the prevention of several types of weld defects (Refs. 18, 19).

Although, these modeling capabilities have been demonstrated in several studies, the models have not been widely used, specially in the industry. An important difficulty is that the model predictions do not

always agree with the experimental results because most phenomenological models lack any built-in component to safeguard the reliability of the model outputs. For example, the computed temperatures do not always agree with the corresponding measured values.

For fusion welding processes, this difficulty has been recognized in the literature. For example, it has been demonstrated (Refs. 20–23) that the reliability of the results obtained from the heat transfer and fluid flow models of fusion welding processes can be enhanced by optimizing values of several uncertain input parameters using a limited volume of experimental data. No similar effort has been reported for the modeling of FSW.

The numerical model of FSW embodies the equations of conservation of mass, momentum, and energy, and the appropriate boundary conditions. The lack of reliability in phenomenological models originates mainly from the other components of the model, i.e., incomplete knowledge and uncertainties in the specification of some of the parameters that describe the friction coefficient between the tool and the workpiece, the extent of slip between the tool and the workpiece, the heat transfer coefficient between the workpiece and the backing plate, and the extent of heat generated by viscous dissipation. If these uncertain welding parameters affect the output significantly, inaccuracy of their values will adversely affect the model results. In other words, if important welding features such as the peak temperature, thermal cycles, and the torque are sensitive to the values of several welding parameters whose values cannot be ascertained accurately, the uncertainty in the values of these parameters would adversely affect the modeling results.

In order for a FSW model output to be

R. NANDAN and T. DEBROY are with Department of Materials Science and Engineering, The Pennsylvania State University, University Park, Pa. B. PRABU and A. DE are with Department of Mechanical Engineering, Indian Institute of Technology Bombay, Powai, Mumbai, India.
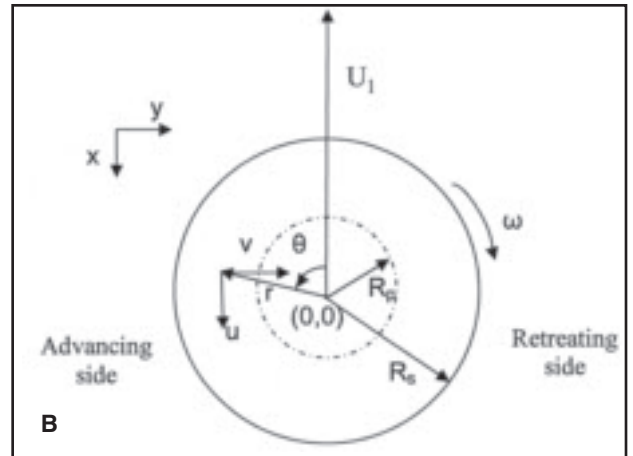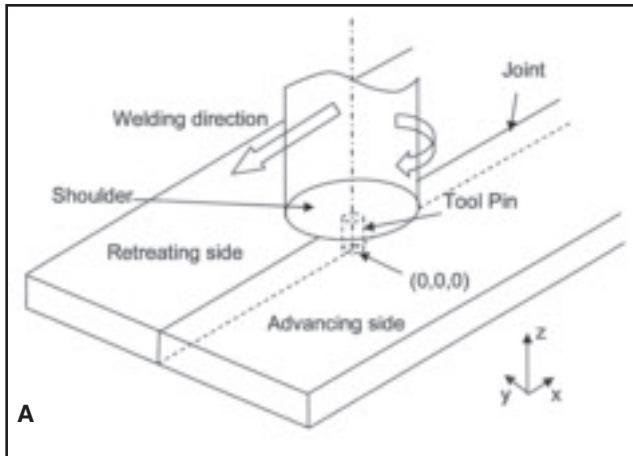
KEYWORDS

Aluminum Welding
Numerical Models
Friction Stir Welding
Plastic Flow
Thermal Cycles
Concentration Profile

Fig. 1 — A — Schematic diagram of the FSW system considered in the model. B — top view of the rotating tool moving in the negative x-direction. θ = 0 corresponds to plane y = 0, x < 0.

Table 1 — Data Used in the FSW Calculations

Property/Weld parameter	Value
Workpiece length (x-direction)	0.45 m
Workpiece half-width (y-direction)	0.07 m
Workpiece thickness	10.0 mm
Shoulder radius	10.0 mm
Pin radius	5.0 mm
Pin length	9.0 mm
Pitch of the thread	1.0 mm
Weld speed	1.05 mm/s
Rotational speed	700–1400 rpm
Axial pressure	18.0 MPa
Tilt angle	0°
Density	2700 kg/m^3
Workpiece materials	AA 1200, AA 6061
Specific heat capacity, (Ref. 34) Cp	
$929.3 - 0.627\,T + 1.48 \times 10^{-3}\,T^2 - 4.33 \times 10^{-8}\,T^{-3}$	J/kg–K
Thermal conductivity, (Ref. 34) k	
$25.2 + 0.398\,T + 7.36 \times 10^{-2}\,T^6 - 2.52 \times 10^{-7}\,T^{-3}$	W/m–K
Tool	
Density	7860–kg/m^3
Specific heat capacity, (Ref. 34) Cp	
$468.3 - 8.5\,T + 3.0 \times 10^{-4}\,T^2 + 1.8 \times 10^{-7}\,T^3$	J/kg-K
Thermal conductivity, (Ref. 34) k	
$3.8 + 9.2 \times 10^{-2}T - 1.8 \times 10^{-4}\,T^2 + 7.8 \times 10^{-8}\,T^3$	W/m-K

as close to the experimental results as possible, the model must have a mechanism to determine the optimized values of these uncertain input parameters within the framework of the phenomenological laws. In the fusion welding processes, a global optimization methodology using a genetic algorithm has been demonstrated to work well for the determination of uncertain welding parameters (Ref. 24).

Here we report the results of a sensitivity study aimed at understanding the roles of friction coefficient, the extent of sticking, heat transfer coefficient at the bottom surface, and the extent of internal heat generation by viscous dissipation on the model output such as the peak temperature, thermal cycles, and the torque. It is shown that all four of these variables significantly affect the FSW model output results. Therefore the values of these parameters are optimized by a genetic algorithm using a limited volume of measured temperatures at several monitoring locations during FSW of dissimilar aluminum alloys AA 1200 and AA 6061. Using the optimized values of the parameters, the computed values of the peak temperatures and the time spans at the base of the thermal cycles at several monitoring loca-

tions are compared with the corresponding experimentally measured values.

Aluminum Alloy AA 6061 contains 0.85 wt-% Mg while AA 1200 contains trace amounts of alloying elements. Hence, a study of FSW of these two alloys provides an excellent way to determine the nature of solute transport, which in turn is related to the plastic flow. Comparison of calculated and experimentally determined concentration profiles of Mg across the weld provides important insight about the nature of plastic flow and mixing of magnesium between the two alloys. The materials flow, temperature fields, cooling rates, torque on the tool, stir zone geometry, and the magnesium concentration profiles are examined for the FSW of AA 1200 and AA 6061 dissimilar aluminum alloys.

Mathematical Model

A schematic diagram of the FSW process is shown in Fig. 1. Friction stir welding of AA 6061 and AA 1200 aluminum alloys was modeled. The dimensions of the plate and the tool used and the thermophysical properties of the workpiece and the tool material (Ref. 25) are given in Table 1. The same thermophysical properties were used for both aluminum alloys. The constitutive equation for flow was the same for the alloys; however, the values of the constants were different.

The plastic flow in three-dimensional Cartesian coordinate system is represented by the momentum conservation equation in index notation, with i = 1, 2, and 3 representing x, y, and z directions, respectively (Refs. 26–29).
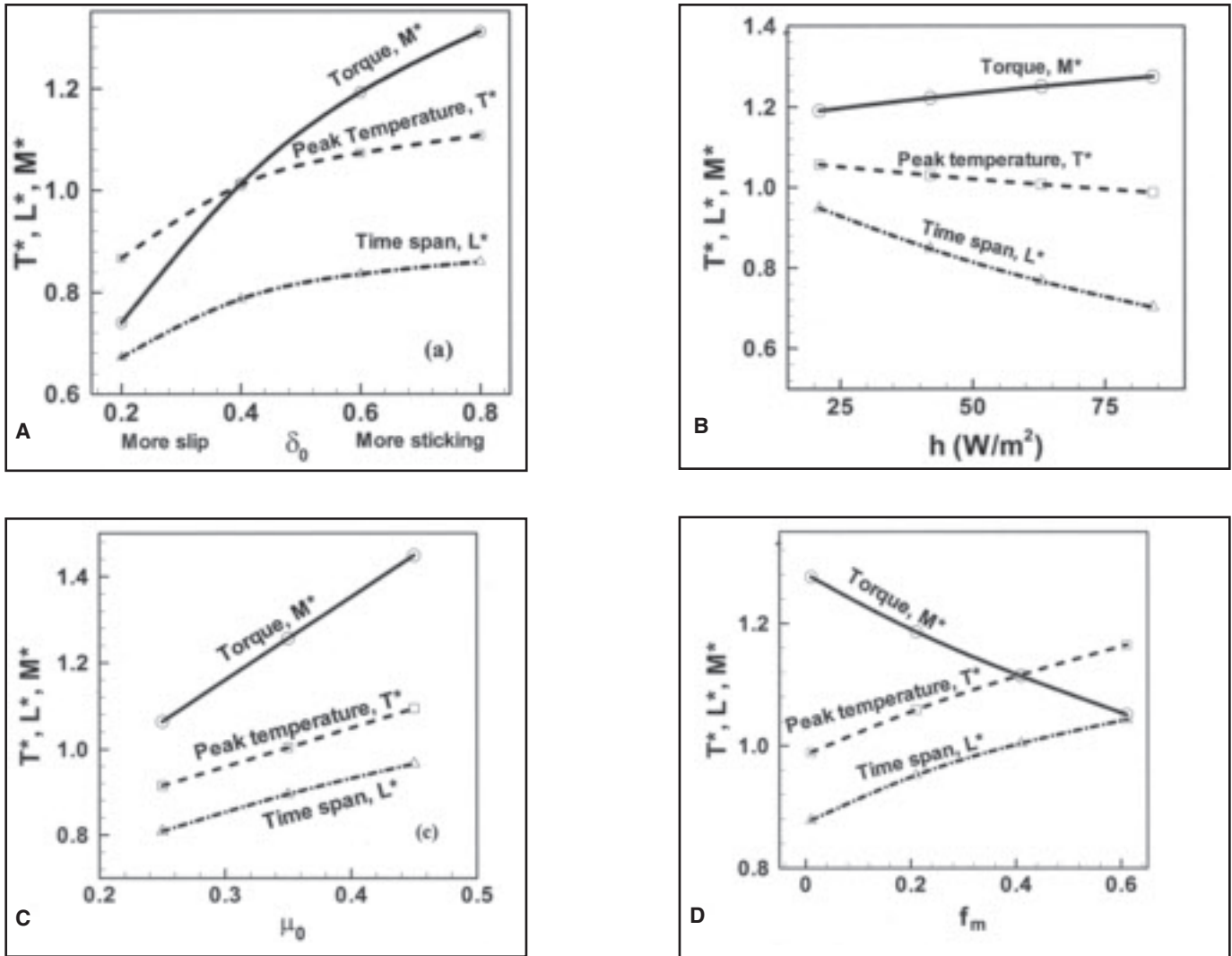
Fig. 2 — Computed dimensionless values of peak temperature, time span at the base of the thermal cycle, and the torque with change in (A) slip, (B) heat transfer coefficient at the bottom, (C) friction coefficient, and (D) multiplicand for viscous dissipation term. In each case, when one of the parameters is varied, other parameters were kept constant. The welding velocity was 0.42 mm/s, and the rotational speed was 450 rev/min.

$$\rho \frac{\partial u_i u_j}{\partial x_i} = -\frac{\partial p}{\partial x_j} + \frac{\partial}{\partial x_i}$$
$$\left(\mu \frac{\partial u_j}{\partial x_i} + \mu \frac{\partial u_i}{\partial x_j} \right) - \rho U_1 \frac{\partial u_j}{\partial x_1} \quad (1)$$

where ρ is the density, μ is the non-Newtonian viscosity, U_1 is the welding velocity, and p is the pressure. Viscosity can be determined from flow stress and effective strain rate as follows (Ref. 30).

$$\mu = \frac{\sigma_e}{3\dot{\varepsilon}} \quad (2)$$

The calculation of viscosity requires local values of strain rate and temperature. The viscosity was calculated based on the following formulation of flow stress, σ_e, proposed by Sheppard and Wright (Ref. 31)

$$\sigma_e = \frac{1}{\alpha} \sinh^{-1} \left[\left(\frac{Z}{A} \right)^{1/n} \right] \quad (3)$$

where A, α, and n are material constant and Z is the Zener-Hollomon parameter. The values of constants A, α, and n are given in Table 2 for AA 6061 and AA 1200 alloys. The Zener-Hollomon parameter, Z, that represents the temperature-compensated effective strain rate is given by

$$Z = \dot{\varepsilon} \exp\left(\frac{Q}{RT} \right) \quad (4)$$

Here Q is the temperature-independent activation energy, R is gas constant, and $\dot{\varepsilon}$ is the effective strain rate given by

$$\dot{\varepsilon} = \left(\frac{2}{3} \varepsilon_{ij} \varepsilon_{ij} \right)^{1/2} \quad (5)$$

where ε_{ij} is the strain rate tensor, defined as

$$\varepsilon_{ij} = \frac{1}{2} \left(\frac{\partial u_i}{\partial x_j} + \frac{\partial u_j}{\partial x_i} \right) \quad (6)$$

This flow-stress model does not have any strain dependency because flow stress is not very sensitive to strain at high temperatures (Ref. 32). Finally, viscosity can be determined from flow stress and effective strain rate from Equation 2. The pressure field was obtained by solving the continuity equation for incompressible single-phase flow simultaneously with the momentum equation

$$\frac{\partial u_i}{\partial x_i} = 0 \quad (7)$$

where u is the velocity of plastic flow. The steady single phase momentum conservation equations with reference to a coordinate system attached to the heat source in index form may be represented as (Refs.
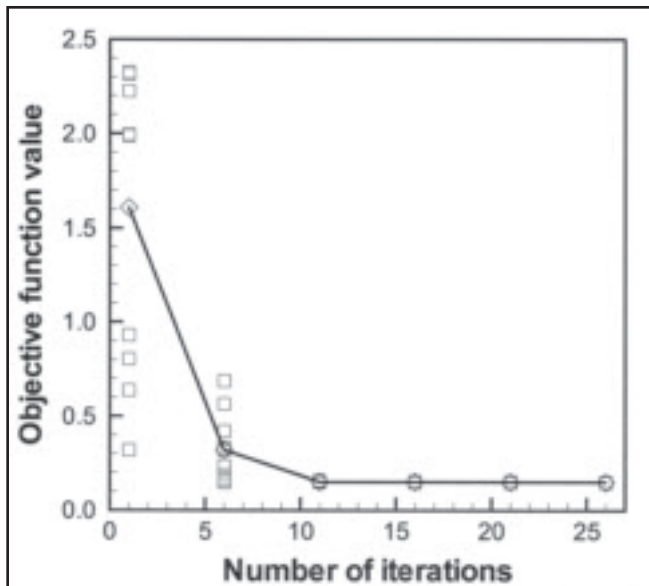
Fig. 3 — Objective function value decreases with iteration. The symbols indicate the objective function values for individual sets of variables, and the line indicates the change in average value of all individuals with successive iterations.

Table 2 — Constants Used in Constitutive Equation for Plastic Flow (Ref. 43)

Alloy	A, s^{-1}	α, (MPa)$^{-1}$	n
6061	2.409×10^8	0.045	3.55
1200	3.902×10^9	0.037	3.84

26–28).

$$\rho C_p \frac{\partial (u_i T)}{\partial x_i} = -\rho C_p U_1 \frac{\partial T}{\partial x_1}$$
$$+ \frac{\partial}{\partial x_i}\left(k \frac{\partial T}{\partial x_i}\right) + S_{in} + S_b \quad (8)$$

where C_p is the specific heat and k is the thermal conductivity of the workpiece/tool. The term S_{in} represents the source term due to interfacial heat generation rate per unit volume at the tool pin-workpiece interface, and S_b is the heat generation rate due to plastic deformation in the workpiece away from the interface. The heat generated at the interface between vertical and horizontal surface of the tool pin and the workpiece, S_{in}, may be defined as (Refs. 26–28)

$$S_{in} = \left[(1-\delta)\eta\tau + \delta\mu_f P \right]$$
$$\left(\omega r - U_1 \sin\theta \right)\frac{A_r}{V} \quad (9)$$

where A_r is any small area on the tool pin-workpiece interface, r is the radial distance of the center of the area from the tool axis, V is the control-volume enclosing the area A_r, τ is the maximum shear stress at yielding, and θ is the angle with the negative x-axis in the counterclockwise direction, η is the mechanical efficiency, i.e., the amount of mechanical energy converted to heat energy, δ denotes the spatially variable fractional slip between the tool and the workpiece interface, μ_f is the spatially variable coefficient of friction, and ω is the angular velocity. Full sticking is indicated by $\delta = 0$. The velocity ($\omega r - U_1$, $\sin\theta$) represents the local velocity of a

point on the tool surface with the origin fixed at the tool-axis. The symbol P is equal to P_U acting on the front half of the cylindrical surface of the pin, and P is equal to P_Z acting on the horizontal surfaces of the tool including both the tool shoulder and pin. The pressure on the tool shoulder and the tool bottom, P_Z, has been assumed to be the same at all points. The pressure on the front half of the cylindrical pin, P_U, is much smaller than P_Z, and has been assumed to be zero.

An estimate of the viscous dissipation of momentum per unit volume, S_b, has been calculated as $f_m\mu\phi$ where ϕ is given by (Ref. 33)

$$\Phi = 2\left(\left(\frac{\partial u_1}{\partial x_1}\right)^2 + \left(\frac{\partial u_2}{\partial x_2}\right)^2 + \left(\frac{\partial u_3}{\partial x_3}\right)^2 \right)$$
$$+ \left(\frac{\partial u_1}{\partial x_2} + \frac{\partial u_2}{\partial x_1}\right)^2 + \left(\frac{\partial u_1}{\partial x_3} + \frac{\partial u_3}{\partial x_1}\right)^2$$
$$+ \left(\frac{\partial u_3}{\partial x_2} + \frac{\partial u_2}{\partial x_3}\right)^2 \quad (10)$$

and f_m is an arbitrary constant that indicates the extent of molecular friction in the system. The value of f_m may tend to 1 for a well-mixed system in molecular scale. In systems where the grains remain largely intact, the value of f_m may be very small. Here, we try to optimize the value of this parameter so that a good agreement can be obtained between the output of the model and physical experiment, thus improving the reliability and usability of the model.

Since the alloys being welded contain different concentrations of Mg, the changes in the concentration of Mg in the two plates due to welding are examined. Apart from 0.85 wt-% Mg AA 6061 alloy also contains other alloying elements. However, for simplicity, it is treated as a binary alloy for modeling purposes. Similarly, AA 1200 is considered to be pure aluminum. We assume no diffusion takes

place into the tool. The equation of conservation of mass of any alloying element present at low concentration is given by

$$\frac{\partial(u_j C_i)}{\partial x_j} = -U_1 \frac{\partial C_i}{\partial x_i} + \frac{\partial}{\partial x_j}\left(D\frac{\partial C_i}{\partial x_j}\right) \quad (11)$$

Here, D denotes temperature-dependent chemical-diffusivity given by

$$D = 0.49 \exp\left(\frac{-124000}{RT}\right) cm^2/s \quad (12)$$

The pre-exponent and activation energy values were obtained from Table 13.4 from *Smithells Metals Reference* book for binary alloy containing 99 at-% Al and 1 at-% Mg (Ref. 34).

The total heat generated at the shoulder/workpiece interface has been partitioned between the workpiece and the tool in the ratio given below (Ref. 35).

$$f = \frac{J_W}{J_T} = \frac{\sqrt{(k\rho C_p)_W}}{\sqrt{(k\rho C_p)_T}} \quad (13)$$

where the subscripts W and T denote the workpiece and the tool, respectively. The analytical expression is based on steady-state one-dimensional heat transfer from point heat source located at the interface of dissimilar metals. The heat flux into the workpiece is estimated to be 90% of the total heat generated. This relation has been examined experimentally by Lienert et al. (Ref. 25) and found to be reliable.

A heat flux continuity at the shoulder matrix interface yields

$$k\frac{\partial T}{\partial z}\bigg|_{top} = \frac{J_w}{J_w + J_T} q_1$$
$$\text{in the range } R_p \le r \le R_s \quad (14)$$

R_P and R_S represent the tool pin and shoulder radius, respectively, and q_1 represents the total rate of heat generation at the shoulder-workpiece interface. It is given by

$$q_1 = \left[\eta(1-\delta)\tau + \delta\mu_f P_T\right]\left(\omega r - U_1 \sin\theta\right) \quad (15)$$

At the bottom surface, there is a backing plate and the heat transfer coefficient from the bottom of the workpiece is not the same as for free convection. The value of the heat transfer coefficient is determined by optimization.
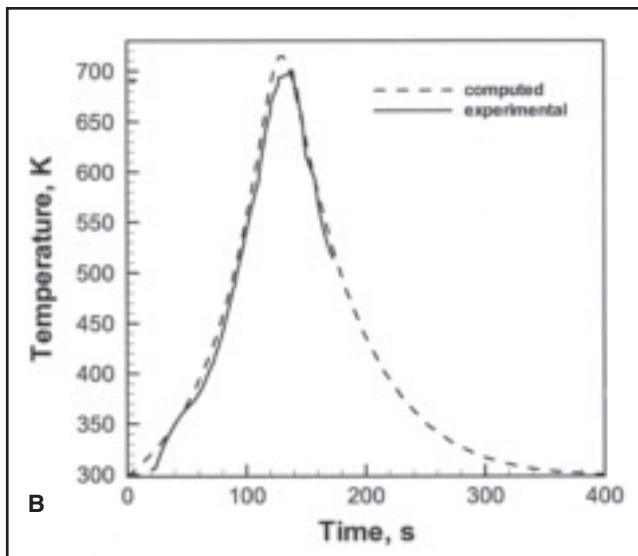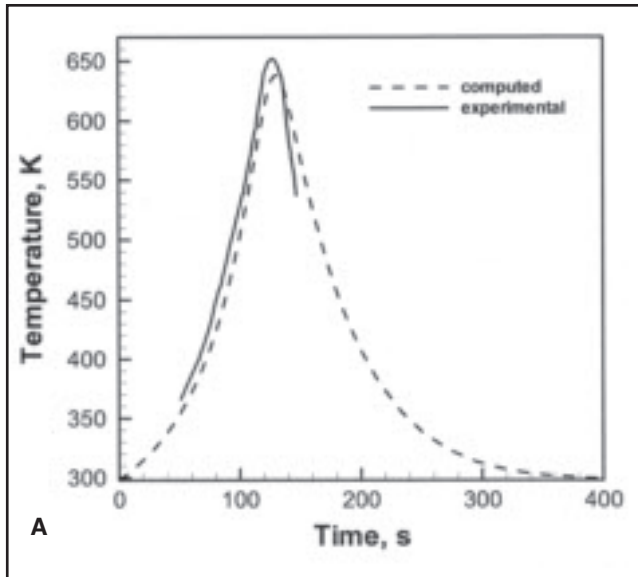
Fig. 4 — Comparison between experimental and calculated time-temperature profile at a point 13 mm away from the centerline on the advancing side. The welding velocity was 1.05 mm/s, and the rotational speed was (A) 710 and (B) 1400 rev/min.
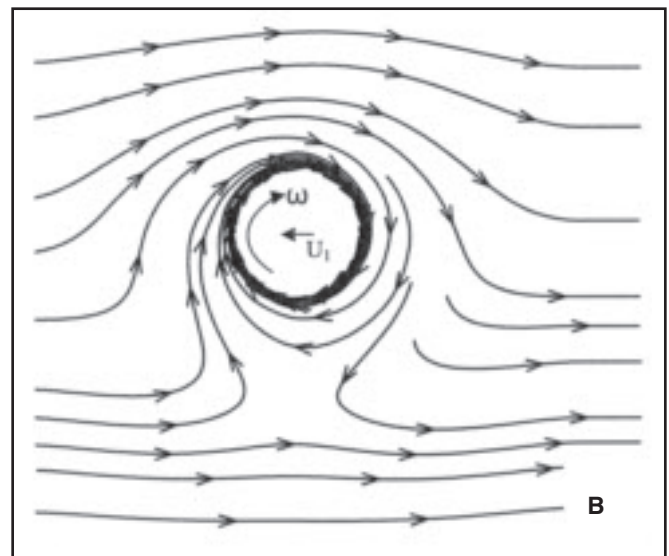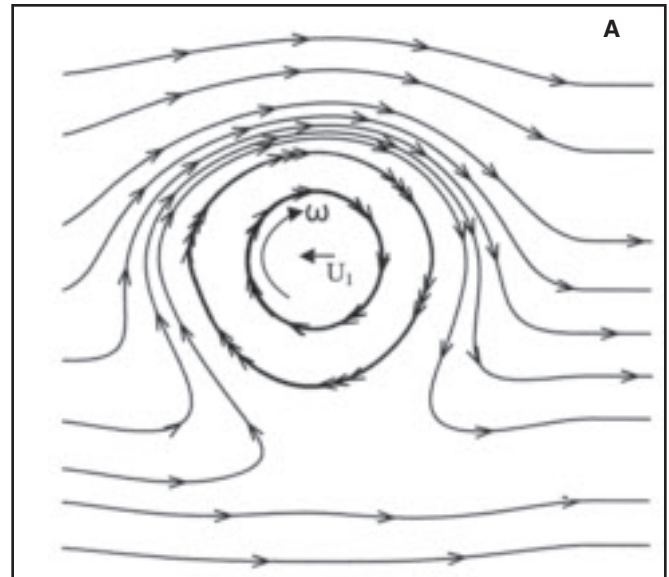

Fig. 5 — Stream-lines in a horizontal plane (A) 3.66 mm and (B) 7 mm below the top surface, showing plastic flow during FSW. Material flows along the retreating side around the pin, and a stagnant zone forms in the advancing side. The welding velocity was 1.05 mm/s and the rotational speed was 710 rev/min.

$$k \frac{\partial T}{\partial z}\bigg|_{bottom} = h_b (T\text{-}T_a) \qquad (16)$$

At the top surface, heat transfer is due to both convection and radiation and is given by

$$k \frac{\partial T}{\partial z}\bigg|_{top} = h_b (T\text{–}T_a) + \sigma (T^4 - T_a^4) \qquad (17)$$

Velocities at the tool pin periphery have been defined in terms of tool translation velocity and the tool pin angular velocity

$$u = (1-\delta)(\omega R_p \sin\theta - U_1)$$
$$v = (1-\delta)\omega R_p \cos\theta$$
$$w = \kappa \frac{\omega}{2\pi} R_p \qquad (18)$$

where κ denotes the pitch of the threads on the cylindrical tool. The value of weld pitch was taken as 1 mm. Similarly, at the shoulder contact, velocity condition may be written as

$$u = (1-\delta)(\omega r \sin\theta - U_1)\Big\}$$
$$v = (1-\delta)\omega r \cos\theta \qquad\Big\}$$
in the range $R_p \le r \le R_s \qquad (19)$

At all other surfaces, temperatures are set to ambient and the velocities are set to zero.

The boundary conditions used for calculation of concentration are straightforward. No flux condition is used for the top and bottom surfaces of the weld plate. The value of concentration is fixed at all other boundaries.

The differential equations of continuity and transport were solved using SIMPLE algorithm (Ref. 36) based solution procedure, capable of calculating three-dimensional heat transfer and fluid flow with a stationary or moving heat source, with a free or flat surface, and well tested
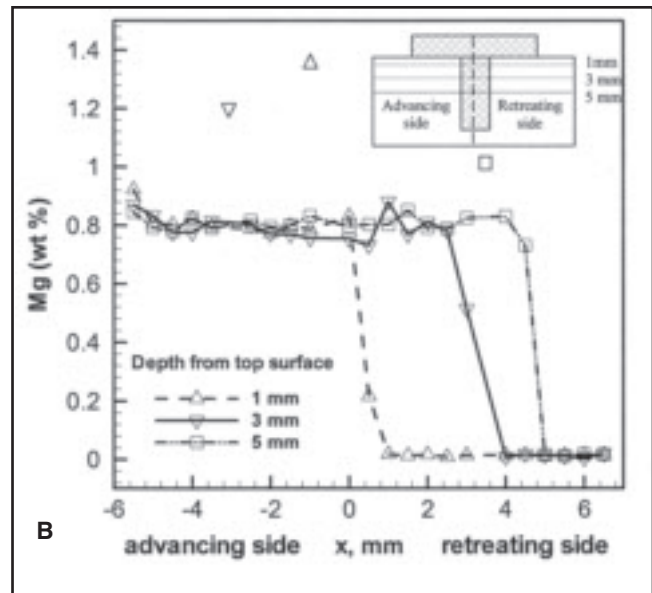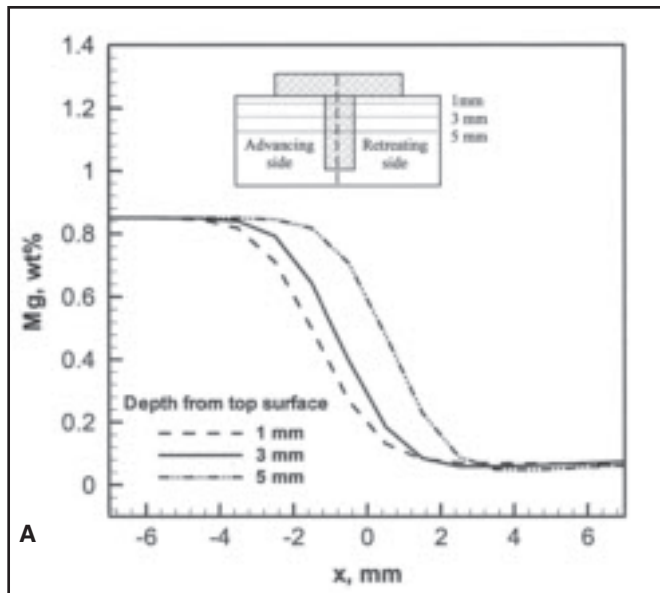
Fig. 6 — Concentration profile at depths of 1, 3, and 5 mm from the top surface, across the weld centerline for AA 6061 (advancing) and AA 1200 (retreating side) weld at 710 rev/min and a weld velocity of 1.05 mm/s. A — Computed; B — measured.
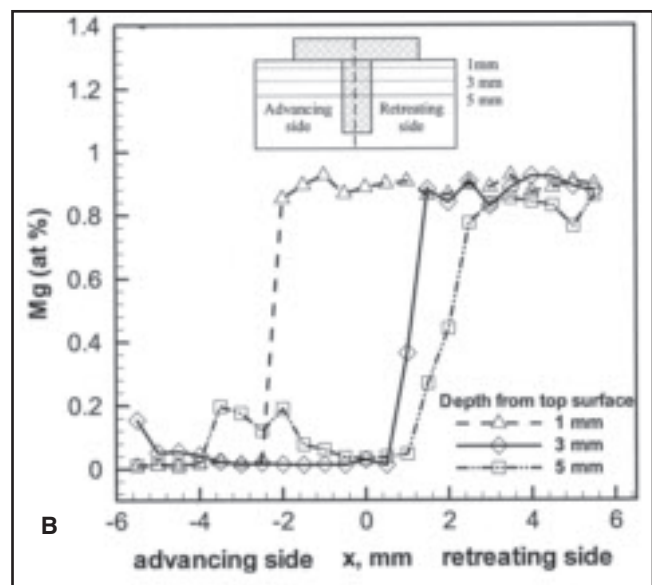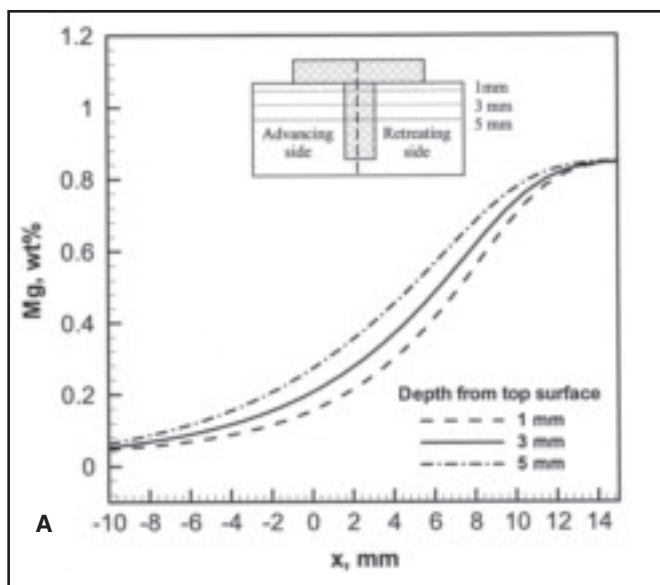

Fig. 7 — Concentration profile at depths of 1, 3, and 5 mm from the top surface, across the weld centerline for AA 1200 (advancing) and AA 6061 (retreating side) weld at 710 rev/min and a weld velocity of 1.05 mm/s. A — Computed; B — measured.

and used for several welding processes.

The trend of the reported data on extent of slip during cross-wedge rolling can be expressed by the following relation (Ref. 37)

$$\delta = 1 - \exp\left(-\delta_0 \frac{\omega}{\omega_0} \frac{r}{R_s}\right) \quad (20)$$

where δ denotes the fraction-slip, and δ_0 is a constant. The above equation was used for all interfaces, with r denoting the distance of the center of the grid-area from the tool axis. It varies from 0 to R_P for the tool pin's bottom surface, is constant at R_P for the vertical surface of the pin, and varies from R_P to R_S for the tool shoulder-workpiece interface. The value of δ_0 was optimized from a limited volume of experimental data. This equation embodies the physical picture of the extent of slip increasing with increase in relative velocity between the tool and the workpiece.

Values of friction coefficient were calculated considering the relative velocity between the tool and the workpiece guided by previous work in the field of friction welding of steel bars (Refs. 38, 39). The relative velocity increases from zero at the axis of rotation (static condition) to ωR_S at the periphery of the tool shoulder (dynamic condition). Experimental evidence in Refs. 37 and 38 suggest that μ has the following form:

$$\mu_f = \mu_0 \exp(-\delta\omega r) \quad (21)$$

where δ is the extent of sticking expressed as a fraction and r is the radial distance from the tool axis for the point in consid-
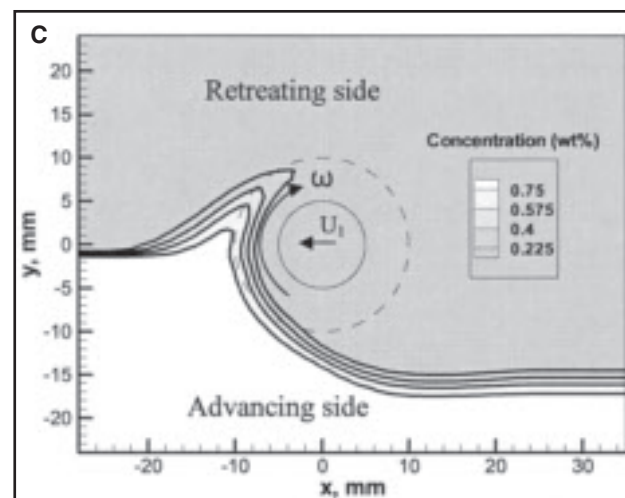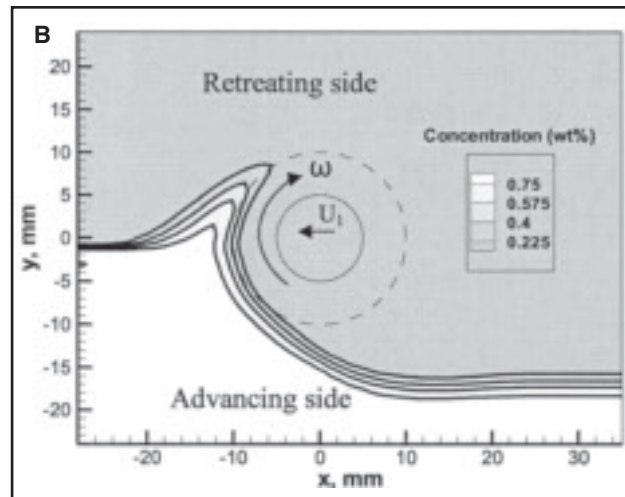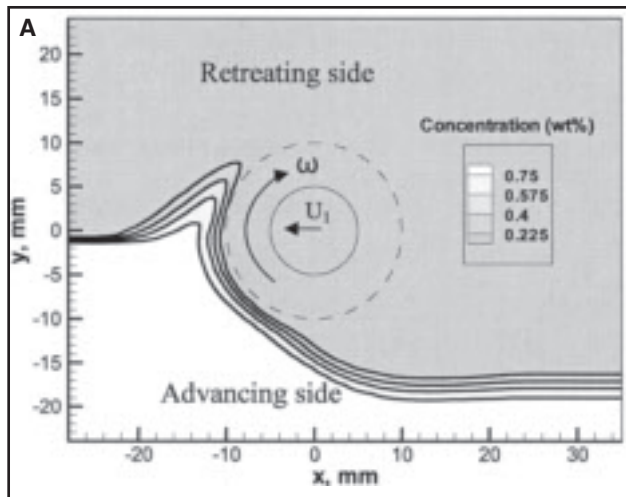
Fig. 8 — Computed concentration profile for magnesium (wt-%) near the tool for AA 1200 (retreating) and AA 6061 (advancing side) weld in horizontal planes corresponding to depths of (A) 1, (B) 3, and (C) 5 mm from the top surface. The rotational speed was 710 rev/min and a welding velocity of 1.05 mm/s.

eration. This equation implies that the friction coefficient decreases with decrease in the relative velocity between the tool and the workpiece.

Optimization of Uncertain FSW Parameters

Among the necessary input variables in the FSW model, there are four uncertain input parameters that affect the reliability of the model output. These parameters are the heat transfer coefficient from the bottom of the workpiece (h), the spatially variable slip between the tool and the workpiece interface (δ), the spatially variable coefficient of friction (μ_f), and the extent of the viscous dissipation term (f_m), which indicates the extent of internal friction in the system. In order to optimize the values of these parameters from a limited volume of experimental data, the following objective function is minimized:

$$O = \sqrt{\sum_{i=1}^{3}\left\{\begin{array}{l}\left(1-Ta_i^*\right)^2+\left(1-Tr_i^*\right)^2\\+\left(1-La_i^*\right)^2+\left(1-Lr_i^*\right)^2\end{array}\right\}} \quad (22)$$

Subscript i denotes different rotational speeds and the subscripts a and r refer to the advancing and the retreating sides, respectively. Two different thermal cycles (at locations 13 mm from the weld centerline on advancing and retreating sides) for each experiment done at 710, 1000, and 1400 rev/min were used to calculate the objective function, i.e., six different thermal cycles were used. The temperature and time span were nondimensionalized using the simple formulas given below

$$T^* = \frac{T_{cal}}{T_{exp}}; \quad L^* = \frac{L_{cal}}{L_{exp}} \quad (23)$$

where T is the peak temperature in the workpiece at a monitoring location 13 mm away from the weld centerline on either advancing or retreating side, and L is the time span on the thermal cycle starting when the temperature reaches 523 K during heating and finishing when the temperature reaches 523 K during cooling at the monitoring location. The normalization of the calculated value is done by the experimental value at the same monitoring location for the same welding condition. The subscripts cal and exp refer to calculated and experimental values, respectively. The objective function value depends on the choice of the four uncertain parameters.

$$O = f\left(h, \mu_0, \delta_0, f_m\right) \quad (24)$$

Differential Evolution (DE), a population-based optimization technique (Refs. 40, 41), was used to optimize the uncertain parameters for FSW.

Results and Discussion

The sensitivities of the computed values of torque on the tool, and peak temperature and cooling time on the four uncertain parameters, identified previously, are examined in Fig. 2A–D. Figure 2A shows that when δ_0 increases and more sticking takes place, torque increases as the tool now moves a larger volume of material during its rotation. Torque is included in the calculations because it affects material flow. Temperatures are higher and the thermal cycles are stronger because of more intense deformational heating consistent with the reduction in frictional heating. Higher temperature leads to longer cooling time.

Figure 2B shows that as the heat transfer coefficient increases, more heat is lost from the workpiece and, therefore, the peak temperature at a distance of 13 mm away from the weld centerline in the advancing side and the time span in the thermal cycle at 523 K decreases. When the heat transfer coefficient is high, lower temperatures result in harder material and higher torque.

Figure 2C shows that the peak temperature and the time span at the base of the thermal cycle increase with increase in friction coefficient due to more intense frictional heating. As the friction between the tool and the workpiece increases, the torque also increases. It offsets the decrease in torque that has been anticipated due to the softening of material with increase in temperature.

Figure 2D shows increase in temperature and cooling time with increase in vis-
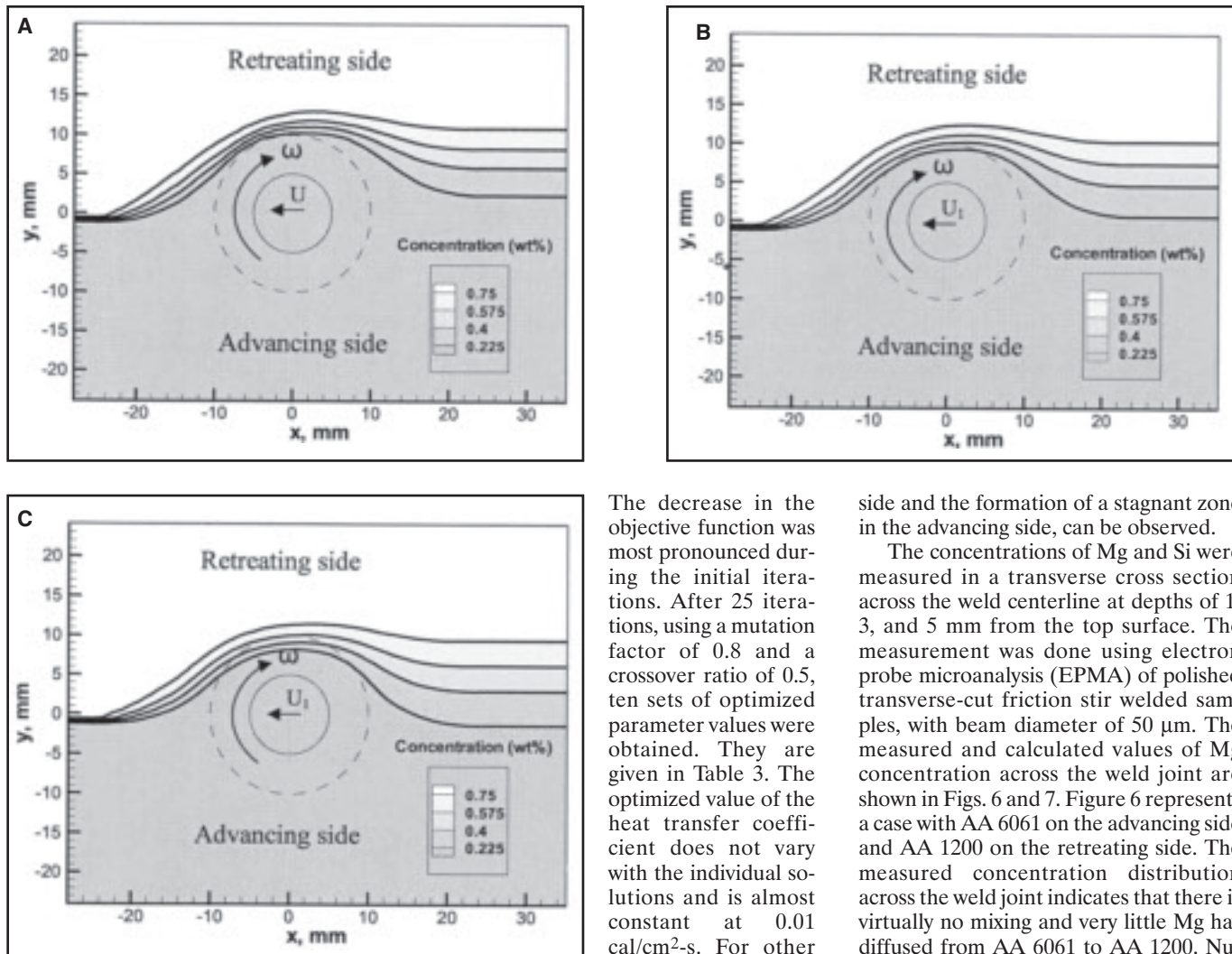
Fig. 9 — Computed concentration profile for magnesium (wt-%) near the tool for AA 1200 (advancing) and AA 6061 (retreating side) weld in horizontal planes corresponding to depths of (A)1, (B) 3, and (C) 5 mm from the top surface. The rotational speed was 710 rev/min, and the weld velocity was 1.05 mm/s.

cous generation of heat that is proportional to f_m. More intense heating results in higher temperatures and softer material, resulting in lower torque.

The results in Fig. 2A–D show that all three output variables, peak temperature, time span at the base of the thermal cycle, and the torque are sensitive to variations in all the four uncertain input variables. Therefore, it is appropriate that all these uncertain input parameters need to be optimized to enhance the reliability of the values of the output variables from the model.

The values of the four uncertain input parameters were optimized using differential evolution (DE) technique. For DE, a population of ten individual sets of four variables was generated. Figure 3 indicates that the average objective function value decreased with successive iterations.

The decrease in the objective function was most pronounced during the initial iterations. After 25 iterations, using a mutation factor of 0.8 and a crossover ratio of 0.5, ten sets of optimized parameter values were obtained. They are given in Table 3. The optimized value of the heat transfer coefficient does not vary with the individual solutions and is almost constant at 0.01 cal/cm²-s. For other variables, we get a range of values depending on the individual solution selected. Since DE is elitist, i.e., the better solution is always picked during selection, we see that diversity of the population steadily decreases.

Figure 4 shows the computed thermal cycle at a distance of 13 mm away from the weld centerline in the advancing side, which used the parametric values obtained through DE, in the heat transfer and plastic flow model. The set of optimized values of the four uncertain parameters that are used in the numerical calculations are given in the second row of Table 3. A close match between the computed temperature-time variation and the corresponding measured values obtained from the thermocouple can be seen in Fig. 4. Using the optimized values of the uncertain parameters, the computed streamlines for the plastic flow are shown in Fig. 5. Two important features of flow, material going around the pin in the retreating

side and the formation of a stagnant zone in the advancing side, can be observed.

The concentrations of Mg and Si were measured in a transverse cross section across the weld centerline at depths of 1, 3, and 5 mm from the top surface. The measurement was done using electron probe microanalysis (EPMA) of polished transverse-cut friction stir welded samples, with beam diameter of 50 μm. The measured and calculated values of Mg concentration across the weld joint are shown in Figs. 6 and 7. Figure 6 represents a case with AA 6061 on the advancing side and AA 1200 on the retreating side. The measured concentration distribution across the weld joint indicates that there is virtually no mixing and very little Mg has diffused from AA 6061 to AA 1200. Numerical results indicate a much larger diffusion distance although the predicted weight-percent of Mg diffusion is similar to the corresponding measured values. The increased movement of Mg from AA 6061 in the advancing side toward AA 1200 in the retreating side with the increase in depth of the workpiece is depicted in both the EPMA measurements and the numerical calculations. In contrast, when AA 6061 was placed on the retreating side, very small amounts of Mg could be traced across the weld joint, except very near to the top surface of the specimen, as indicated in Fig. 7. The calculated trends in Mg concentrations across the weld joint (Fig. 7A) are slightly different from the corresponding measured results (Fig. 7B) when Mg-containing alloy (AA 6061) is on the advancing side. Although the reason for this mismatch is not clearly known, the calculations assume molecular level mixing in the plasticized material whereas in the experiments, the grains are deformed but remain largely intact.

Contours of concentration of Mg near the tool are shown in Figs. 8 and 9, at dif-

ferent depths from the top surface. It is observed from these figures that Mg is drawn toward the direction of rotation of the tool, in front of the tool. Just below the tool shoulder, the plug of material flowing around the tool is larger. Material is transported from the rear of the tool to the front in the advancing side. Hence the region where plastic flow has occurred becomes depleted in Mg and therefore the front of the tool is rich in Mg. At the middle horizontal plane, the circular plug of material around the tool is smaller and hence the high concentration region is closer to the tool pin.

The concentration profiles, with Mg on the advancing side, are qualitatively similar to experimental results for Ti-marker flow in FS-welded AA 2024, studied by Zettler et al. (Ref. 42) using high-resolution (20 µm) computer microtomography. The tomographic volume data are shown in Fig. 10. Zettler et al. also observed that when the marker was placed in the advancing side, it redistributed as fine particulates, while the marker placed on the retreating side appeared as much larger clumps. This could be the reason for the concentration calculations, with Mg on the retreating side, not reconciling with the corresponding experimental results.
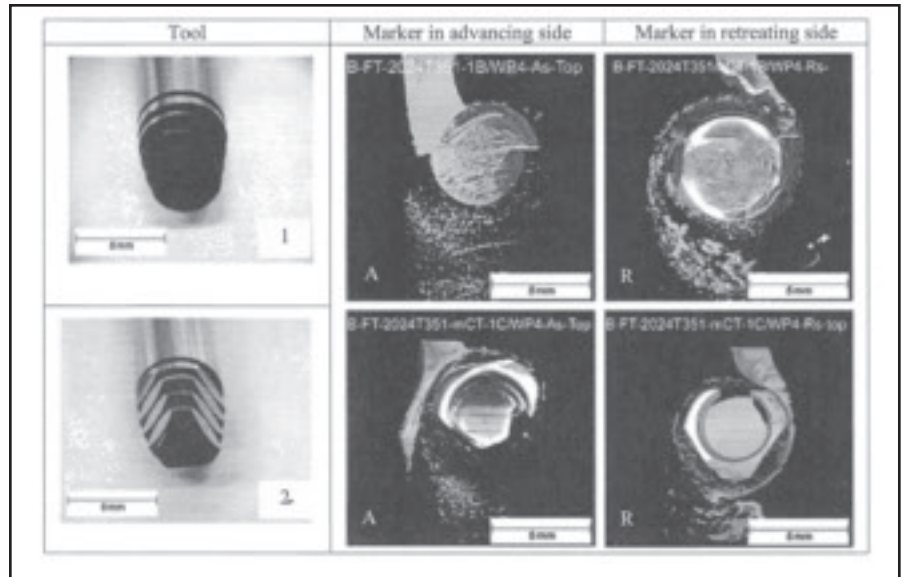

Fig. 10 — Tomographic volume data depicting Ti-marker flow in AA 2024 T351 alloy with two different tool pins: 1. conical and threaded; and 2. conical, threaded with flats. The markers were placed in both A) advancing and R) retreating sides (Ref. 42).

Summary and Conclusions

Heat transfer, materials flow, mixing and energy necessary for the friction stir welding of dissimilar aluminum Alloys AA 1200 and AA 6061 were studied both experimentally and theoretically. The special features of the work and the main findings of this investigation are the following:

1) A numerical model embodying the equations of conservation of mass, momentum, and energy was used to examine the sensitivity of four important parameters, which are friction coefficient, the extent of slip between the tool and the workpiece, the heat transfer coefficient at the bottom of the workpiece, and the extent of viscous dissipation converted to heat on the computed temperature fields and torque on the tool. These parameters cannot be prescribed either from the welding conditions or from fundamental principles. All four parameters were found to significantly affect both the temperature fields and the torque on the tool.

2) When the values of these four uncertain parameters were optimized using a small volume of experimental data, the computed peak temperature, thermal cycle, and the torque on the tool agreed very well with the corresponding experimental data.

3) The transport and mixing of magnesium from Mg-rich AA 6061 alloy into very low alloy containing AA 1200 were examined both experimentally by EPMA and numerically in the entire volume of the three-dimensional specimens. The measured concentration profiles showed that the mixing of magnesium did not occur in the atomic level and the spatial variation of concentration distribution showed a step profile between the two plates. The computed magnesium concentration profile based on its transport by convection and diffusion showed a gradual decrease from 0.85% Mg in AA 6061 to very small concentration in AA 1200. The comparison of the experimental and computed concentration profiles showed imperfect mixing of the plasticized alloys during FSW where the materials seem to move in layers without significant diffusive interlayer mixing.

4) For the conditions of experiments reported here, the cooling rates were of the order of about 5 K/s in the 700 to 500 K temperature range. The relatively low cooling rate is consistent with fairly high energy input per unit length.

5) The small value of the extent of slip between the tool and the workpiece obtained by optimization procedure indicates close to sticking condition, even at the outer periphery of the tool shoulder.

6) The optimized extent of viscous dissipation converted to heat is small consistent with the fact that the grains in the

Table 3 — Optimized Sets of Uncertain Parameters after 25 Iterations and the Corresponding Objective Functions

Friction Coefficient μ_0	Fractional Slip δ_0	Heat Transfer Coefficient h (cal/cm²-s)	Efficiency of Mixing f_m	Objective Function O
0.488	0.022	0.010	0.036	0.149
0.487	0.014	0.010	0.03	0.148
0.484	0.014	0.010	0.028	0.148
0.482	0.017	0.011	0.034	0.149
0.479	0.016	0.011	0.033	0.148
0.489	0.012	0.010	0.029	0.150
0.49	0.015	0.010	0.032	0.148
0.492	0.012	0.012	0.033	0.150
0.499	0.010	0.012	0.031	0.149
0.499	0.017	0.010	0.031	0.149

workpiece are deformed but largely retain their identity after welding.

7) The torque values and the interfacial heat generation rate were computed from shear stress. Therefore, the close agreement between the experimentally measured and the calculated thermal cycles and torque values indicates that the computed shear stress at the tool-workpiece interface is accurate and the optimization of uncertain parameters provide reliable computed results.

References

1. Zhang, W., Kim, C. L., and DebRoy, T. 2004. *Journal of Applied Physics*, 95(9): 5210–5219.

2. Rai, R., and DebRoy, T. 2006. *Journal of Physics, D: Applied Physics*, 39(6): 1257–66.

3. Yang, Z., Sista, S., Elmer, J. W., and Deb Roy, T. 2000. *Acta Materialia*, 48(20): 4813–4825.

4. Mishra, S., and DebRoy, T. 2004. *Acta Materialia*, 52(5): 1183–1192.

5. Sista, S., and DebRoy, T. *Metallurgical and Materials Transactions, B*, 32(6): 1195–1201.

6. Mishra, S., and DebRoy, T. 2004. *Journal of Physics D: Applied Physics*, 37: 2191–2196.

7. Elmer, J. W., Palmer, T. A., Zhang, W., Wood, B., and DebRoy, T. 2003. *Acta Materialia*, 51(12): 3333–3349.

8. Zhang, W., Elmer, J. W., and DebRoy, T. 2002. *Materials Science and Engineering* A, 333(1-2): 320–335.

9. Mundra, K., DebRoy, T., Babu, S. S.,and David, S. A. 1997. *Welding Journal*, 76(4): 163-s to 171-s.

10. Hong, T., Pitscheneder, W., and DebRoy, T. 1998. *Science and Technology of Welding and Joining*, 3(1): 33–41.

11. Mundra, K., and DebRoy, T. 1993. *Metallurgical Transactions, B*, 24(1): 145–155.

12. Collur, M. M., and DebRoy, T. 1989. *Metallurgical Transactions, B*, 20(2): 277–286.

13. DebRoy, T., Basu, S., and Mundra, K., 1991. *Journal of Applied Physics*, 70(3): 1313–1319.

14. Miller, R., and DebRoy, T. 1990. *Journal of Applied Physics*, 68(5): 2045–2050.

15. He, X., DebRoy, T., and Fuerschbach, P. W. 2003. *Journal of Applied Physics,* 94(10): 6949–6958.

16. Mundra, K., Blackburn, J. M., and DebRoy, T. 1997. *Science and Technology of Welding and Joining*, 2(4): 174–184.

17. Mundra, K., and DebRoy, T. 1995. *Metallurgical and Materials Transactions B*, 26(1): 149–157.

18. Zhao, H., and DebRoy, T. 2003. *Journal of Applied Physics*, 93(12): 10089–10096.

19. Basu, T., and DebRoy, T. 1992. *Journal of Applied Physics,* 72(8): 3317–3322.

20. De, S. A., and DebRoy, T. 2006. *Science and Technology of Welding and Joining*, 11(2): 143–153.

21. De, A., and DebRoy, T. 2005. *Welding Journal,* 84(7): 101-s to 112-s.

22. De, A., and DebRoy, T. 2004. *Journal of Physics, D: Applied Physics*, 37: 140–150.

23. De, A., and DebRoy, T. 2004. *Journal of Applied Physics*, 95(9): 5230–5239.

24. Mishra, S., and DebRoy, T. 2005. *Journal of Applied Physics*, 98(4): No. 044902.

25. Lienert, T. J., Stellwag, W. L. Jr., Grimmett, B. B., and Warke, R. W. 2003. *Welding Journal*, 82: 1-s to 9-s.

26. Nandan, R., Roy, G. G., and DebRoy, T. 2006. *Metallurgical and Materials Transactions A*, 37: 1247–1259.

27. Nandan, R., Roy, G. G., Lienert, T. J., and DebRoy, T. 2006. *Science and Technology of Welding and Joining*, 11: 526–537.

28. Nandan, R., Roy, G. G., Lienert, T. J., and DebRoy, T. 2007. *Acta Materialia*, 55(3): 883–895.

29. Nandan, R., Roy, G. G., and DebRoy, T. 2006. *Sci. Technol. Weld. Joining*, 11: 606–608.

30. Zienkiewicz, O. C., and Cormeau, I. C. 1974. *International Journal of Numerical Methods in Engineering*, Vol. 8: 821–845.

31. Sheppard, T., and Wright, D. S. 1979. *Metals Technology*, Vol. 6: 215–223.

32. Seo, S., Min, O., and Yang, H. 2005. *International Journal of Impact Engineering*, Vol. 31: 735–754.

33. Bird, R. B., Stewart, W. E., and Lightfoot, E. N. 2000. *Transport Phenomena*, John Wiley and Sons, New York, p. 82.

34. Brandes, E. A., and Brook, G. B. 1999. *Smithells Metals Reference Book*, 7th ed., Butterworth-Heinemann, Oxford, UK.

35. Carslaw, H. S., and Jaeger, J. C. 1959. *Conduction of Heat in Solids*, Clarendon Press, Oxford, UK.

36. Patankar, S. V. 1980. *Numerical Heat Transfer and Fluid Flow*, Hemisphere Publishing Corp., New York.

37. Deng, Z., Lovell, M. R., and Tagavi, K. A. 2001. *Journal of Manufacturing Science and Engineering*, 123: 647–653.

38. Kong, H. S., and Ashby, M. F. 1991. MRS Bulletin, Vol. 8.

39. Vill, V. I. 1962. *Friction Welding of Metals*, AWS, Reinhold, N.Y.

40. Storn, R., and Price, K. 1995. *Differential Evolution — A Simple and Efficient Adaptive Scheme for Global Optimization over Continuous Spaces*, Technical Report TR-95-012, ICSI.

41. Price, K., Storn, R., and Lampinen, J. 2005. *Differential Evolution — A Practical Approach to Global Optimization*, Springer, Berlin.

42. Zettler, R., Donath, T., Dos Santos, J. F., Beckman, F., and Lohwasser, D. 2006. *Advanced Engineering Materials*, 8: 487–490.

43. Sheppard, T., and Jackson, A. 1997. *Materials Science and Technology*, 13(3): 203–209.